



A Genetic Algorithm to Model Solar Radio Active Regions From 3D Magnetic Field Extrapolations

Alexandre José de Oliveira e Silva^{1,2,3}, Caius Lucius Selhorst^{1*}, Joaquim E. R. Costa³, Paulo J. A. Simões^{4,5}, Carlos Guillermo Giménez de Castro^{4,6}, Sven Wedemeyer⁷, Stephen M. White⁸, Roman Brajša⁹ and Adriana Valio⁴

¹NAT–Núcleo de Astrofísica, Universidade Cidade de São Paulo, São Paulo, Brazil, ²IP&–Instituto de Pesquisa e Desenvolvimento, Universidade do Vale do Paraíba, São José dos Campos, Brazil, ³INPE–Instituto Nacional de Pesquisas Espaciais (DICEP), São José dos Campos, Brazil, ⁴Centro de Rádio Astronomia e Astrofísica Mackenzie, Escola de Engenharia, Universidade Presbiteriana Mackenzie, São Paulo, Brazil, ⁵SUPA School of Physics and Astronomy, University of Glasgow, Glasgow, United Kingdom, ⁶Instituto de Astronomía y Física del Espacio, CONICET-UBA, Ciudad Universitaria, Buenos Aires, Argentina, ⁷Roseland Centre for Solar Physics, Institute of Theoretical Astrophysics, University of Oslo, Oslo, Norway, ⁸Space Vehicles Directorate, Air Force Research Laboratory, Albuquerque, NM, United States, ⁹Hvar Observatory, Faculty of Geodesy, University of Zagreb, Zagreb, Croatia

OPEN ACCESS

Edited by:

Masumi Shimojo,
National Astronomical Observatory of
Japan (NINS), Japan

Reviewed by:

Sijje Yu,
New Jersey Institute of Technology,
United States
Victor De La Luz,
National Autonomous University of
Mexico, Mexico

*Correspondence:

Caius L. Selhorst
caiuslucius@gmail.com

Specialty section:

This article was submitted to
Stellar and Solar Physics,
a section of the journal
Frontiers in Astronomy and Space
Sciences

Received: 02 April 2022

Accepted: 06 May 2022

Published: 16 June 2022

Citation:

de Oliveira e Silva AJ, Selhorst CL,
Costa JER, Simões PJ,
Giménez de Castro CG,
Wedemeyer S, White SM, Brajša R and
Valio A (2022) A Genetic Algorithm to
Model Solar Radio Active Regions
From 3D Magnetic
Field Extrapolations.
Front. Astron. Space Sci. 9:911118.
doi: 10.3389/fspas.2022.911118

In recent decades our understanding of solar active regions (ARs) has improved substantially due to observations made with better angular resolution and wider spectral coverage. While prior AR observations have shown that these structures were always brighter than the quiet Sun at centimeter wavelengths, recent observations at millimeter and submillimeter wavelengths have shown ARs with well defined dark umbrae. Given this new information, it is now necessary to update our understanding and models of the solar atmosphere in active regions. In this work, we present a data-constrained model of the AR solar atmosphere, in which we use brightness temperature measurements of NOAA 12470 at three radio frequencies: 17, 100 and 230 GHz. The observations at 17 GHz were made by the Nobeyama Radioheliograph (NoRH), while the observations at 100 and 230 GHz were obtained by the Atacama Large Millimeter/submillimeter Array (ALMA). Based on our model, which assumes that the radio emission originates from thermal free-free and gyroresonance processes, we calculate radio brightness temperature maps that can be compared with the observations. The magnetic field at distinct atmospheric heights was determined in our modelling process by force-free field extrapolation using photospheric magnetograms taken by the Helioseismic and Magnetic Imager (HMI) on board the Solar Dynamics Observatory (SDO). In order to determine the best plasma temperature and density height profiles necessary to match the observations, the model uses a genetic algorithm that modifies a standard quiet Sun atmospheric model. Our results show that the height of the transition region (TR) of the modelled atmosphere varies with the type of region being modelled: for umbrae the TR is located at 1080 ± 20 km above the solar surface; for penumbrae, the TR is located at 1800 ± 50 km; and for bright regions outside sunspots, the TR is located at 2000 ± 100 km. With these results, we find good agreement with the observed AR brightness temperature maps. Our modelled AR can be used to estimate the emission at frequencies without observational coverage.

Keywords: Sun: radio radiation, Sun: atmosphere, Sun: magnetic fields, force-free field extrapolation, Sun–active regions

1 INTRODUCTION

Numerous semi-empirical models of the solar atmosphere are intended to reproduce solar active region (AR) observations with success in a specific wavelength range. Most of these efforts have been based on optical and UV line observations (e.g.: Vernazza et al., 1981; Fontenla et al., 1993, 1999, 2009) and have had success modelling the observations at these wavelengths. Nevertheless, these models are less successful in reproducing radio observations of ARs, perhaps due to the presence of distinct emission mechanisms at radio wavelengths and the lack of comparable spatial resolution.

In the last decades our knowledge of solar active regions has improved substantially due to observations made with better angular resolution. Recent observations at millimeter and submillimeter wavelengths have shown ARs with well defined dark umbrae (Loukitcheva et al., 2014; Iwai and Shimojo, 2015; Shimojo et al., 2017). Moreover, Iwai et al. (2016) suggested that even at radio frequencies as low as 34 GHz the observed brightness temperature (T_b) of the umbral region is almost the same as that of the quiet region, which indicates that the height (and therefore temperature) in the atmosphere at which its emission becomes optically thick should be lower than that predicted by the models.

Great advances in the understanding of AR behavior have been acquired with the daily NoRH (Nakajima et al., 1994) observations at 17 GHz since 1992, and also 34 GHz after 1996. Vourlidis et al. (2006) studied 529 ARs observed by the NoRH at 17 GHz (1992–1994), and concluded that the ARs with polarization greater than 30% contain a gyroresonance core that increases their brightness temperatures to $T_b \geq 10^5$ K, well above the quiet Sun brightness temperature ($T_{b, QS}$) of 10000 K at 17 GHz. Moreover, they also argued that these high T_b values were due to opacity at the gyroresonance 3rd harmonic, requiring 2000 G of magnetic field intensity ($|\vec{B}|$) in the corona, and therefore at least $|\vec{B}| = 2200$ G at the photospheric level.

At submillimeter wavelengths, Silva et al. (2005) analyzed a total of 23 ARs observed during 2002 at 212 and 405 GHz from the Submillimeter Solar Telescope (SST, Kaufmann et al., 2008) and combined with maps at 17 and 34 GHz from NoRH. The flux density spectra at these frequencies was found to increase with frequency with a slope of 2, indicating that the emission from these active regions is predominantly due to thermal bremsstrahlung. Moreover, Valle Silva et al. (2021) made a similar analyses with the inclusion of the ALMA single-dish data reaching the same conclusions.

Further advances in the study of ARs became possible in 2016, with the start of ALMA observations at millimeter/submillimeter wavelengths (Wedemeyer et al., 2016). During the Science Verification period, 2015 December 16–20, AR 12470, including a sunspot umbra, was observed by the ALMA interferometric array at Band 3 (84–116 GHz) and Band 6 (211–275 GHz). Whereas the sunspot umbra exhibited a continuous dark region at Band 6 (Shimojo et al., 2017), at Band 3 the center of the umbra showed a

bright structure with T_b 800 K above the dark region around it (Iwai et al., 2017). This Band 3 brightness enhancement may be an intrinsic feature of the sunspot umbra at chromospheric heights, such as a manifestation of umbral flashes, or it could be related to a coronal plume.

Selhorst et al. (2008) were able to reproduce the brightness temperatures and the spatial structure of AR NOAA 10008 seen in NoRH observations at 17 and 34 GHz. That work used photospheric magnetic field extrapolation to derive \vec{B} in the atmosphere¹ and suggested that the AR chromospheric temperature and density gradients were steeper than those proposed for the quiet Sun. Also, the temperature and density in the corona needed to be greater than expected in the quiet Sun, as expected. With these assumptions, the model was able to reproduce the high T_b observed in the 17 GHz gyroresonance core, and also the free-free emission observed in non-polarized areas at both 17 and 34 GHz.

Brajša et al. (2009) studied active regions observed at 37 GHz with the 14-m antenna of the Metsähovi Radio Observatory and compared the measured intensities with radiation models. They concluded that thermal bremsstrahlung can explain the observed radiation of ARs, while thermal gyromagnetic emission can, with high probability, be excluded as a possible radiation mechanism at the frequency considered (37 GHz). Further, Brajša et al. (2018) compared intensities measured in full-disc solar ALMA maps taken at 248 GHz with model-based prediction of the brightness temperatures. Again, they concluded that the thermal bremsstrahlung is the main radiation mechanism responsible for the AR emission, also at this observing frequency (248 GHz).

As an improvement of the AR modelling presented in Selhorst et al. (2008, 2009), in this work we apply a genetic algorithm (GA; Charbonneau, 1995) to modify a standard quiet Sun atmospheric model in order to determine the best plasma temperature and density height profiles necessary to match the observations of NOAA 12470 obtained by ALMA (single-dish maps at 100 and 230 GHz) and NoRH (17 GHz interferometric map).

Finally, we note that Brajša et al. (2020) performed a preliminary analysis of the magnetic structure above the same AR 12470 using LOS photospheric magnetograms and a potential-field source surface (PFSS) model to extrapolate magnetic fields into the solar chromosphere and corona. Results of the model were compared with the ALMA single-dish (248 GHz) and interferometric (100 GHz) measurements of the same AR. The general extrapolated magnetic structure is consistent with the ALMA observations, but a detailed analysis and comparison with ALMA small-scale features was not possible with the model used and requires a more detailed magnetic field extrapolation model, what is performed in the present work.

¹The 3D magnetic field extrapolation used in Selhorst et al. (2008) has been integrated in the fast algorithm GX Simulator tool available in SolarSoft (Nita et al., 2015, 2018).

2 ATMOSPHERIC MODELLING VIA GENETIC ALGORITHM

The purpose of this study is to estimate the temperature and electron density as a function of height in the solar atmosphere, as constrained by brightness temperature T_b maps of radio observations. The different frequencies provide access to different layers of the atmosphere due to the frequency dependence of opacity. An initial 1D atmospheric model is used as a seed for the GA: at each step, T_b is obtained via the calculation of radiative transfer incorporating opacity from both the thermal bremsstrahlung and gyroresonance emission mechanisms. For these calculation, the 3D magnetic field structure above the AR is derived from linear force-free extrapolations (LFF) from photospheric magnetograms. The GA iteratively updates the atmospheric plasma trapped by magnetic field lines until a best model is found via χ^2 minimization of the calculated and observed T_b values. This process is run independently for each pixel of the observed radio maps, resulting in an atmospheric model (T and n versus height) for each line of sight. Together, the results for all pixels provide the 3D atmospheric model for the active region.

2.1 Genetic Algorithm Features

In order to determine the best plasma temperature and density height profiles necessary to match the observations, we employ the genetic algorithm Pikaia (Charbonneau, 1995).

The atmospheric model developed by Selhorst et al. (2005b, hereafter SSC) is used as the seed in the genetic algorithm, that changes the seed model to find the best fit for the observational measurements. Five free parameters are supplied to the GA representing the atmospheric model. These parameters are based on the ideas presented in Selhorst et al. (2008), as follows:

- ∇T —changes the AR temperature gradient in the chromosphere;
- ∇n_e —changes the AR electron density gradient in the chromosphere;
- N_T —changes the AR coronal temperature by a constant value, in which $N_T = \frac{T_{AR}}{T_{qS}}$;
- N_{n_e} —changes the AR coronal electron density by a constant value, in which $N_{n_e} = \frac{n_{eAR}}{n_{eqS}}$;
- Δh —changes the TR position.

These five free parameters combined build new electron density and temperature profiles, which are used, along with the magnetic field values for the line-of-sight column, to calculate the bremsstrahlung and gyroresonance absorption coefficients. The radiative transfer is then performed and the resulting T_b values are compared with the observations. Nevertheless, the GA used here is a mathematical solution and it does not verify if the atmospheric plasma is in local thermodynamic equilibrium (LTE) or not.

A generation of child atmospheric models is created by the algorithm based on the parent models with the lowest χ^2 values, using the genetic algorithm described in Charbonneau (1995). The GA starts with the choice of minimum and maximum values

for each one of the five free parameters. The method used here was full-generation replacement using ten generations with one hundred children each. The crossover probability was 0.85 and the mutation mode was variable. The initial mutation rate, that is, the initial probability that any gene locus will mutate in any generation, was 0.005. Finally, the mutation rate range was between 0.0005 and 0.25. In our runs the χ^2 measure typically stabilizes to a minimum value by about the seventh generation.

2.2 Magnetic Field Extrapolation

Photospheric magnetograms are used as the boundary condition for an extrapolation of the field above the photosphere using the linear force-free field approximation. The fundamental equation that describes a force-free field (assuming that the current density is parallel to the magnetic field at any point in space) is

$$\vec{\nabla} \times \vec{B} = \alpha \vec{B} \quad (1)$$

where α is a proportionality function and represents the current density distribution, called a force-free function.

The extrapolation routine is based on the works of Nakagawa and Raadu (1972) and Seehafer (1978) and was previously implemented in IDL by J. E. R. Costa and T. S. N. Pinto (used in Selhorst et al., 2005a, 2008; Nita et al., 2018). The calculation starts from the line-of-sight magnetic field component at the photosphere and determines the magnetic field above it for both the potential field ($\alpha = 0$) and the force-free field ($\alpha \neq 0$). The result is three cubes of intensities, one for each component of the magnetic field vector (B_x , B_y , and B_z) and another data cube for the positions of the magnetic field lines. The positions of the magnetic field lines determine where the atmospheric plasma is changed with respect to the quiet Sun. Moreover, the x and y dimensions of the cubes have the same dimensions as the selected active region area. In this work, the extrapolated field lines were calculated only above positions with $|\vec{B}|_{\min} = 200$ G at the photosphere. A different minimum value could be chosen by the user, but we found that the inclusion of magnetic fields below this limit resulted in the simulated ARs appearing much larger than the observed ARs. This approach in effect determines one parameter, i.e., the lower limit of the field strength needed to best reproduce the observations.

2.3 Emission Mechanisms

The brightness temperature T_b is obtained by computing the radiative transfer along the line of sight for each column of the AR. At radio frequencies, in the quiescent solar atmosphere, the main emission mechanisms are bremsstrahlung and gyroresonance (Dulk, 1985). The thermal bremsstrahlung absorption coefficient (κ_b) is calculated by

$$\kappa_b \approx 9.78 \times 10^{-3} \frac{n_e}{\nu^2 T^{3/2}} \sum_i Z_i^2 n_i \times g(T, \nu) \quad (2)$$

where ν is the observed frequency (Hz), T is the plasma temperature and n_e is the electron density. Only the contributions of collisions with protons was considered, since its density is much larger than that of other ion species (n_i).

Following Zirin (1988), it was assumed $Z = 1.178$, if a fully hydrogen atmosphere was considered, i.e., $Z = 1$, the resulting T_b should be only $\sim 3\%$ smaller for all frequencies simulated here.

The Gaunt factor ($g(T, \nu)$) used is as follow:

$$g(T, \nu) = \begin{cases} 18.2 + \ln T^{3/2} - \ln \nu & (T < 2 \times 10^5 \text{K}) \\ 24.5 + \ln T - \ln \nu & (T > 2 \times 10^5 \text{K}) \end{cases}$$

The gyroresonance absorption coefficient (κ_g) is

$$\begin{aligned} \kappa_g(s, \theta) &= \int_{-\infty}^{\infty} \kappa_g(s, \theta) \frac{d\nu}{\nu_b} \\ &= \left(\frac{\pi}{2} \right)^{\frac{5}{2}} \frac{2}{c} \frac{\nu_p^2}{\nu} \frac{s^2}{s!} \left(\frac{s^2 \beta_o^2 \sin^2 \theta}{2} \right)^{s-1} \times (1 - \sigma |\cos \theta|)^2 \end{aligned} \quad (3)$$

where $\sigma = +1$ for the o-mode and $\sigma = -1$ for the x-mode, $\beta_o^2 = kT/mc^2$. The harmonic is defined as $s = \nu/\nu_B$, where ν_B is electron-cyclotron frequency and ν_p is the electron plasma frequency:

$$\begin{aligned} \nu_B &\approx 2.8 \times 10^6 B \\ \nu_p &\approx 9000 n_e^{1/2} \end{aligned} \quad (4)$$

Since the contribution of higher harmonics to the radio emission is very small (Shibasaki et al., 1994), the gyroresonance emission was only calculated for harmonics smaller than 5 ($s \leq 5$).

Following Zirin (1988), radiative transfer yields the brightness temperature as a function of wavelength as:

$$T_b(\nu) = \int T \kappa_\nu e^{-\tau_\nu} dL \quad (4)$$

where $\kappa_\nu = \kappa_b + \kappa_g$, dL is the distance element towards the observer, and τ_ν is the optical depth

$$\tau_\nu = \int \kappa_\nu dL \quad (5)$$

3 OBSERVATIONS

In this work, we selected the active region AR NOAA 12470 to test our algorithm. This region was selected due to the availability of radio observations at three frequencies: 17 GHz, from the Nobeyama Radio Heliograph (NoRH), 100 and 230 GHz from the Atacama Large Millimetric and submillimetric Array (ALMA) (Shimojo et al., 2017; Valle Silva et al., 2021).

Here, the LFF extrapolations algorithm used the line-of-sight (LOS) magnetogram obtained by the Helioseismic and Magnetic Imager (HMI, Schou et al., 2012) on the Solar Dynamics Observatory (SDO, Pesnell et al., 2012), nevertheless, the LFF extrapolations could also be applied to vector magnetograms. HMI operates at wavelengths around 6173 Å (Fe I) and provides LOS magnetograms of 4096 × 4096 pixels with ~ 0.5 arcsec spatial resolution.

3.1 Magnetogram

Figure 1A shows the HMI line of sight (LOS) magnetogram obtained on 17 December 2015 at 14:51 UT. This full Sun image has an apparent radius of 975" and magnetic field intensities ($|\vec{B}|$) up to 2300 G. The active region is shown in detail in Figure 1B, centered in the point of greatest magnetic field intensity ($|\vec{B}|_{\max}$). The selected area included the whole AR NOAA 12470, and also part of the AR NOAA 12469 located to the northwest of the central umbra.

The line-of-sight magnetogram will underestimate field strengths in AR 12470 due to projection effects, since the region is significantly offset from disk center. To correct for this, the AR has been rotated to solar disk center, solar spherical curvature has been removed, and the magnetic field intensities have been corrected for projection. This increases the maximum field strength from 2,300 G to ~ 2500 G.

3.2 Radio Maps

The ALMA maps used here were obtained during the Science Verification period, 2015 December 16–20². The maps were obtained by the fast-scan single-dish method described in White et al. (2017), at Band 3 (84–116 GHz) and Band 6 (211–275 GHz). Following Selhorst et al. (2019), we took 100 and 230 GHz as the reference frequencies for Bands 3 and 6, respectively. The maps were made from observations of a 12 m diameter antenna, resulting in nominal spatial resolutions of 25" and 58" at 230 and 100 GHz, respectively.

Since the radio maps were not obtained at the same time as the magnetogram, it was necessary to take into account solar rotation when aligning the radio data with the magnetogram. The nominal time of the 230 GHz map is 14:52 UT, i.e., only 1 min difference from the nominal time of the HMI observation, requiring just -0.01° of longitudinal rotation. The nominal time of the 100 GHz map was 19:35 UT, requiring a longitudinal rotation of -2.85° . Moreover, the ALMA maps come in distinct sizes, 800 × 800 pixels² (3" pixel) at 230 GHz and 400 × 400 pixels² (6" pixel) at 100 GHz. Thus for a better comparison with the model results they were resized to match the HMI magnetogram (4096 × 4096 pixels²).

While the quiet Sun brightness temperature ($T_{b,qs}$) at 230 GHz is 6210 ± 110 K (Selhorst et al., 2019), the AR 12470 brightness temperature (T_b) varies from 5800 to 6600 K across locations with magnetic field intensities greater than 1500 G, i.e., the minimum intensity to form a sunspot (Livingston et al., 2012). At 100 GHz, $T_{qs} = 7,110 \pm 90$ K (Selhorst et al., 2019) and AR 12470 showed T_b varying from 7,200 to 7,650 K where $|\vec{B}| > 1500$ G.

We also used 17 GHz radio maps obtained routinely by NoRH with resolution of 10–18 arcsec in intensity and circular polarization (Nakajima et al., 1994) and intensity maps at 34 GHz with 5–10" spatial resolution (Takano et al., 1997). We used a 17 GHz map observed at 02:44 UT and available in 512 × 512 pixels² format (4.91" resolution), rotated longitudinally by 7.31° with respect to the HMI magnetogram. At 17 GHz, T_{qs}

²<https://almascience.eso.org/alma-data/science-verification>.

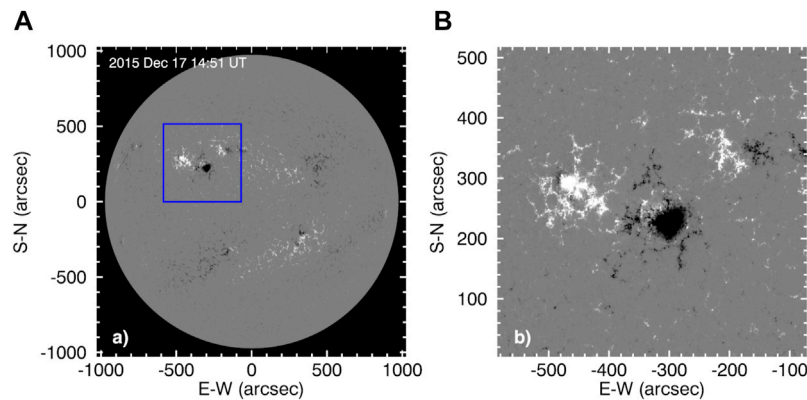


FIGURE 1 | The (A) image shows the SDO/HMI LOS magnetogram obtained on 2015 December 17 at 14:51 UT. The blue rectangle indicates the selected area of active region AR12470, shown in expanded form in the (B). The region shown is $516.4'' \times 516.4''$, centered at $17.40''N, 17.68''E$.

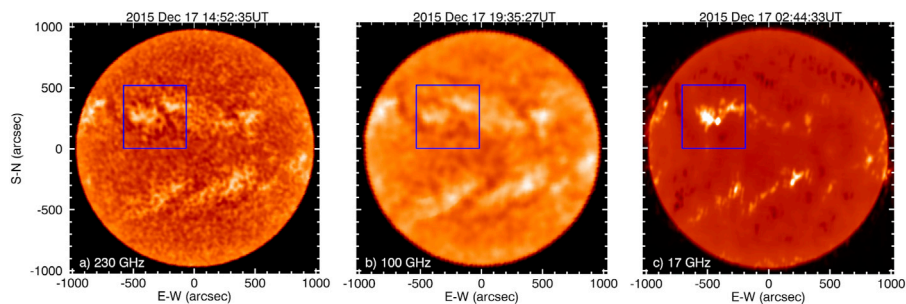


FIGURE 2 | Full disc solar maps obtained at (A) 230 GHz (A), (B) 100 GHz and (C) the NoRH map at 17 GHz. The blue rectangle in each panel indicates the selected area of the active region AR12470, taking into account solar rotation given timing differences relative to the HMI magnetogram.

$= 10050 \pm 120$ K, and AR 12470 has brightness temperatures varying from 5.3×10^4 to 6.8×10^4 K in the areas with $|\vec{B}| > 1500$ G. **Figure 2** shows the ALMA single dish maps obtained at 230 and 100 GHz, plus the NoRH map at 17 GHz. In contrast to the small levels of variability in the ALMA maps, at 17 GHz the active region T_b reached values almost 7 times the level of the quiet Sun. The bright compact source in the active region has a high polarization degree ($\sim 100\%$) indicating the presence of a gyroresonance core (Vourlidis et al., 2006; Selhorst et al., 2008) which is coincident with the sunspot umbra.

4 RESULTS

A low value for the α parameter in (1) does not significantly affect the extrapolated magnetic field configuration at low heights in the atmosphere: here $\alpha = -0.005$ was chosen for the LFF extrapolation since it generated a greater number of closed magnetic field lines in the selected region than did the potential-field extrapolation ($\alpha = 0$). **Figure 3** shows some of the magnetic field lines obtained in the extrapolation with $\alpha = -0.005$ and $|\vec{B}|_{\min} = 200$ G.

To speed up the computational process, the datacubes and images were resized from 1024×1024 pixels² to 256×256 pixels², corresponding to a spatial resolution $\sim 2''$ per pixel. However, the radiative transfer calculations require better resolution in the height of the voxels (h_z) due to the relatively narrow width of the chromosphere, and they were re-scaled via interpolation from the resolution of the magnetogram to 50 km, similar to the resolution of the SSC model.

The GA optimizes the electron density and temperature profiles for each vertical column in the model cube by comparing the brightness temperatures obtained from the model with the observed maps, pixel by pixel. This procedure initially generated ~ 28 thousand different atmosphere profiles. These profiles were refined, in order to reduce the χ^2 between observed T_b values and those obtained from the model. The final model is obtained when the χ^2 from the GA process ceases to reduce further.

The resulting atmospheric profiles were grouped into four different classes corresponding to different atmospheric features: umbrae, penumbrae, plage and quiet Sun. To speed up the GA process, distinct initial seeds were used for each class. Each pixel in the magnetogram was classified as umbra, penumbra, or plage according to its intensity ($|\vec{B}|$), as follows: umbra, $|\vec{B}| \geq 1500$ G

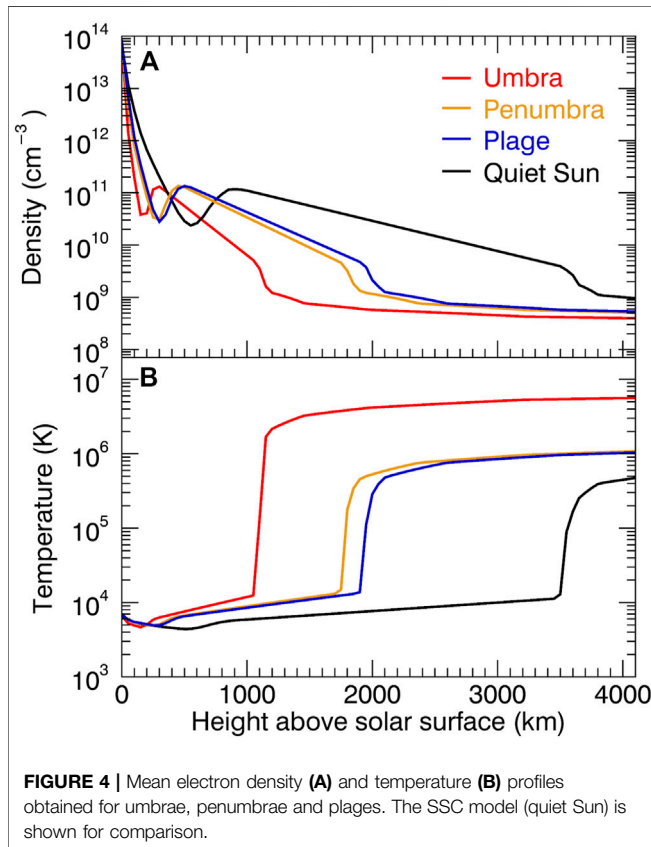
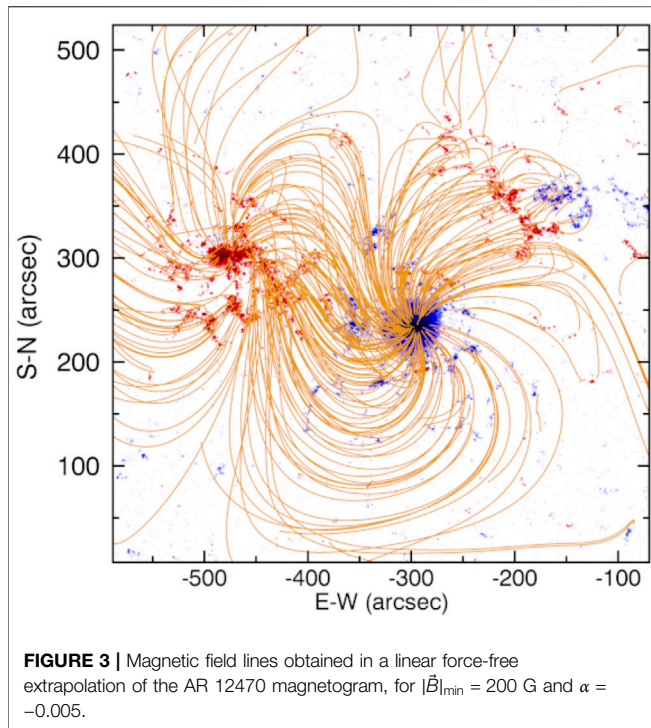


TABLE 1 | Average transition region heights in models of distinct atmospheric features.

AR region	$ \vec{B} _0$ (G)	TR height (km)
Quiet Sun	$ \vec{B} _0 < 200$	3,500
Umбра	$ \vec{B} _0 \geq 1500$	1080 ± 20
Penumbra	$1000 \leq \vec{B} _0 < 1500$	1800 ± 50
Plages	$200 \leq \vec{B} _0 < 1000$	2000 ± 100

(~ 200 pixels); penumbra, $1000 \leq |\vec{B}|_0 < 1500$ G (~ 230 pixels); plages, $200 \leq |\vec{B}|_0 < 1000$ G ($\sim 27,200$ pixels). All pixels with $|\vec{B}| \leq 200$ G were classified as quiet Sun ($\sim 38,000$ pixels) and were assumed to have $T_B = T_{qS}$. We then obtained the average electron density and temperature profiles for each of the three AR classes by calculating the average of the profiles with the lowest χ^2 values in the T_b calculation, in relation to the observed values at the three distinct observing frequencies. These resulting models are shown in **Figure 4** along with the SSC quiet Sun, for comparison.

The $|\vec{B}|$ limits used to classify each pixel are based on studies by Livingston et al. (2012), who derived a minimum necessary value of 1500 G for sunspot formation. Moreover, the umbra is a compact source with a diameter $\sim 25''$ in its largest part. In Nita et al. (2018), the authors proposed a similar separation, however, in that work the separation was based on solar white light images instead of a magnetogram, which is not useful for faint or spotless ARs.

In **Table 1** we present the average height of the transition region (TR), which is one of the five free parameters fitted in the GA process, for each atmospheric class: thus, 1080 ± 20 km above the solar surface for umbrae, 1800 ± 50 km for penumbrae, and $2,000 \pm 100$ km for plages.

4.1 Free-Free Contribution

The GA is able to derive appropriate fits for the assumed basic structure of the solar atmosphere, i.e., fitting for the 5 free parameters yields satisfactory models. Although, the SSC model considers the plasma fully ionized above 1,000 km, i.e. $n_e = n_i$, to simplify the GA the densities were grouped in a single variable, that is $(n_e \times n_i)^{1/2}$. This variable was assumed as the density in **Table 2** and **Figure 4**. **Table 2** shows the variation of temperature and density as function of height for the distinct AR areas, moreover, the distinct atmospheric layer were displayed in different colors, that is salmon for photosphere, green for chromosphere and orange for TR and corona.

Comparison with the quiet-Sun model indicates that the umbrae, penumbrae and plages have a narrower temperature-minimum region and a thinner chromosphere than the quiet Sun, as can be seen in **Table 2** and **Figure 4**. Moreover, the compression of the temperature minimum and the chromosphere are most pronounced in umbral pixels, i.e., the region with more intense magnetic fields (**Figure 4**). The mean umbral model placed the transition region close to 1,000 km above the solar surface, in agreement with previous work (e.g., Fontenla et al., 1999, 2009; Selhorst et al., 2008; Nita et al., 2018, see also; Zlotnik et al., 1996). Furthermore, the umbral region is

TABLE 2 | Variation of temperature and density as function of height for the distinct AR areas. The distinct atmospheric layer were displayed in different colors, that is salmon for photosphere, green for chromosphere and orange for TR and corona.

Height (km)	Quiet Sun		Plage		Penumbra		Umbra	
	Temperature (K)	Density $[(n_e \times n_i)^{1/2}]$ (cm^{-3})	Temperature (K)	Density $[(n_e \times n_i)^{1/2}]$ (cm^{-3})	Temperature (K)	Density $[(n_e \times n_i)^{1/2}]$ (cm^{-3})	Temperature (K)	Density $[(n_e \times n_i)^{1/2}]$ (cm^{-3})
0.0	6.5200E+03	6.7882E+13	6.9568E+03	7.9951E+13	6.9568E+03	8.0156E+13	6.6786E+03	8.0079E+13
100.0	5.4100E+03	3.7211E+12	5.4831E+03	1.1535E+12	5.4236E+03	7.8583E+11	4.9185E+03	1.9381E+11
200.0	4.9900E+03	6.5751E+11	5.1178E+03	1.2238E+11	5.0417E+03	8.2822E+10	5.0368E+03	4.0661E+10
300.0	4.7700E+03	2.0174E+11	4.9405E+03	2.7854E+10	5.0807E+03	3.0434E+10	6.2980E+03	1.3120E+11
400.0	4.5600E+03	6.9649E+10	5.8022E+03	7.6292E+10	6.1542E+03	1.0840E+11	6.9067E+03	8.5847E+10
500.0	4.4071E+03	2.8640E+10	6.5441E+03	1.3471E+11	6.6928E+03	1.2788E+11	7.5747E+03	5.5659E+10
600.0	4.5500E+03	2.6229E+10	6.9024E+03	1.1233E+11	7.0932E+03	9.8027E+10	8.2983E+03	3.6027E+10
700.0	5.0045E+03	5.2452E+10	7.2778E+03	8.8068E+10	7.5130E+03	7.5063E+10	9.0839E+03	2.3368E+10
800.0	5.4690E+03	9.4091E+10	7.6690E+03	6.8978E+10	7.9529E+03	5.7486E+10	9.9380E+03	1.5132E+10
900.0	5.7445E+03	1.1679E+11	8.0776E+03	5.4071E+10	8.4148E+03	4.4031E+10	1.0867E+04	9.8165E+09
1000.0	5.9000E+03	1.1000E+11	8.5048E+03	4.2397E+10	8.9001E+03	3.3727E+10	1.1879E+04	6.3579E+09
1100.0	6.0573E+03	9.6271E+10	8.9519E+03	3.3208E+10	9.4106E+03	2.5837E+10	1.3144E+05	3.5132E+09
1200.0	6.2188E+03	8.4253E+10	9.4201E+03	2.6047E+10	9.9479E+03	1.9794E+10	2.1610E+06	1.2177E+09
1300.0	6.3847E+03	7.3736E+10	9.9106E+03	2.0422E+10	1.0514E+04	1.5164E+10	2.5885E+06	1.0404E+09
1400.0	6.5549E+03	6.4532E+10	1.0425E+04	1.5996E+10	1.1109E+04	1.1618E+10	3.0181E+06	8.6324E+08
1500.0	6.7297E+03	5.6477E+10	1.0964E+04	1.2552E+10	1.1737E+04	8.9018E+09	3.3377E+06	7.4682E+08
1600.0	6.9092E+03	4.9427E+10	1.1529E+04	9.8406E+09	1.2398E+04	6.8206E+09	3.5101E+06	7.1085E+08
1700.0	7.0934E+03	4.3257E+10	1.2122E+04	7.7100E+09	1.3095E+04	5.2261E+09	3.6829E+06	6.7492E+08
1800.0	7.2825E+03	3.7857E+10	1.2744E+04	6.0504E+09	1.3711E+04	3.2130E+09	3.8559E+06	6.3902E+08
1900.0	7.4767E+03	3.3132E+10	1.3806E+04	4.7408E+09	1.4365E+04	1.3433E+09	4.0292E+06	6.0316E+08
2000.0	7.6761E+03	2.8996E+10	1.4887E+04	3.537E+08	1.5035E+04	1.1619E+09	4.1805E+06	5.7397E+08
2100.0	7.8808E+03	2.5377E+10	1.5919E+04	2.613E+08	1.5744E+04	1.0535E+09	4.2745E+06	5.6185E+08
2200.0	8.0909E+03	2.2209E+10	1.7009E+04	1.9487E+08	1.6453E+04	9.4510E+08	4.3686E+06	5.4974E+08
2300.0	8.3067E+03	1.9437E+10	1.8181E+04	1.4048E+08	1.7160E+04	8.3678E+08	4.4626E+06	5.3765E+08
2400.0	8.5282E+03	1.7010E+10	1.9371E+04	1.0513E+08	1.7867E+04	7.5280E+08	4.5566E+06	5.2557E+08
2500.0	8.7556E+03	1.4887E+10	2.0561E+04	8.5237E+08	1.8576E+04	7.3078E+08	4.6507E+06	5.1349E+08
2600.0	8.9890E+03	1.3029E+10	2.1815E+04	7.5985E+08	1.9285E+04	7.0878E+08	4.7448E+06	5.0143E+08
2700.0	9.2287E+03	1.1402E+10	2.3064E+04	6.7363E+08	2.0000E+04	6.8679E+08	4.8389E+06	4.8937E+08
2800.0	9.4748E+03	9.9791E+09	2.4313E+04	6.0406E+08	2.0715E+04	6.6481E+08	4.9330E+06	4.7733E+08
2900.0	9.7275E+03	8.7335E+09	2.5564E+04	5.4630E+08	2.1430E+04	6.4285E+08	5.0271E+06	4.6529E+08
3000.0	9.9868E+03	7.6433E+09	2.6813E+04	4.9200E+08	2.2145E+04	6.2090E+08	5.1213E+06	4.5325E+08
3100.0	1.0253E+04	6.6892E+09	2.8062E+04	4.4181E+08	2.2860E+04	5.9897E+08	5.2155E+06	4.4122E+08
3200.0	1.0527E+04	5.8542E+09	2.9311E+04	3.9443E+08	2.3575E+04	5.7704E+08	5.3098E+06	4.2920E+08
3300.0	1.0807E+04	5.1235E+09	3.0560E+04	3.5126E+08	2.4290E+04	5.6817E+08	5.3552E+06	4.2413E+08
3400.0	1.1095E+04	4.4839E+09	3.1809E+04	3.1267E+08	2.5005E+04	5.6076E+08	5.3896E+06	4.2060E+08
3500.0	1.1291E+04	3.9172E+09	3.3058E+04	2.7746E+08	2.5715E+04	5.5335E+08	5.4239E+06	4.1709E+08
3600.0	1.1492E+04	3.4258E+09	3.4307E+04	2.4875E+08	2.6425E+04	5.4595E+08	5.4581E+06	4.1357E+08
3700.0	1.1697E+04	3.0000E+09	3.5556E+04	2.2484E+08	2.7135E+04	5.3854E+08	5.4922E+06	4.1006E+08
3800.0	1.1902E+04	2.6250E+09	3.6805E+04	2.0483E+08	2.7845E+04	5.3115E+08	5.5263E+06	4.0655E+08
3900.0	1.2107E+04	2.2999E+09	3.8054E+04	1.8632E+08	2.8555E+04	5.2376E+08	5.5602E+06	4.0304E+08
4000.0	1.2312E+04	2.0250E+09	3.9303E+04	1.6979E+08	2.9265E+04	5.1637E+08	5.5941E+06	3.9953E+08
4250.0	1.2717E+04	1.5000E+09	4.1802E+04	1.3526E+08	3.0775E+04	4.9791E+08	5.6786E+06	3.9078E+08
4500.0	1.3122E+04	1.1250E+09	4.4301E+04	1.0075E+08	3.2280E+04	4.7948E+08	5.7628E+06	3.8203E+08
4750.0	1.3527E+04	8.0000E+08	4.6800E+04	7.0200E+07	3.3785E+04	4.6107E+08	5.8466E+06	3.7330E+08
5000.0	1.3932E+04	6.0000E+08	4.9300E+04	5.0000E+07	3.5290E+04	4.4267E+08	5.9301E+06	3.6457E+08
5250.0	1.4337E+04	4.5000E+08	5.1800E+04	3.5000E+07	3.6795E+04	4.2486E+08	6.0135E+06	3.5585E+08
5500.0	1.4742E+04	3.2500E+08	5.4300E+04	2.5000E+07	3.8300E+04	4.1947E+08	6.0966E+06	3.4714E+08
5750.0	1.5147E+04	2.2500E+08	5.6800E+04	1.8000E+07	3.9805E+04	4.1409E+08	6.1795E+06	3.3844E+08
6000.0	1.5552E+04	1.5000E+08	5.9300E+04	1.3000E+07	4.1310E+04	4.0872E+08	6.2623E+06	3.2975E+08

the only one that presents a significant increase in the coronal temperature, which is necessary to reach the high T_b values observed in the gyroresonance source at 17 GHz (Selhorst et al., 2008, 2009).

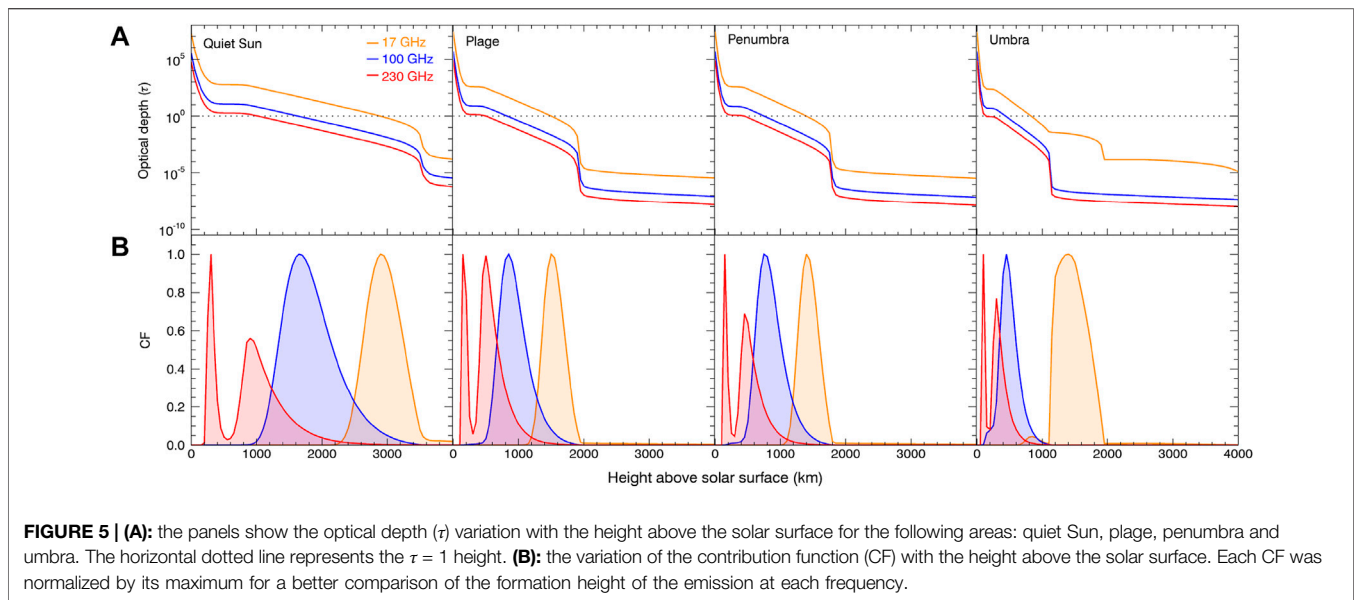
In **Figure 5** we show, for each atmospheric class, the optical depth (τ , A row) and the contribution function (CF, B row), that represents the emission variation with the atmosphere height. The CF is defined as

$$CF(h) = j_\nu e^{-\tau_\nu} \quad (6)$$

where $j_\nu = \kappa_\nu B_\nu(T)$ is the emission coefficient, and $B_\nu(T)$ is the Planck function. Following Tapia-Vázquez and De la Luz (2020), each CF shown in **Figure 4** was normalized by its maximum, for a

better comparison of the formation height of the emission at each frequency.

As previously reported by Selhorst et al. (2019), the quiet Sun free-free emission at 230 GHz is formed mainly in two different layers: near the temperature-minimum region ($h \sim 400$ km), and in the chromosphere, with a peak around 900 km. Moreover, the contraction of the atmosphere does not change the CF double-peak structure, rather it just changes the heights of the two peaks and their contribution percentages (see red curves in **Figure 5**). On the other hand, the quiet Sun free-free emission at 100 and 17 GHz are completely formed in the chromosphere, with CF peaks, respectively, at 1,650 and 2,900 Km. These heights of the maximum of the CF are close to the atmosphere height at which τ



= 1, as expected. Moreover, the atmospheric reduction of the AR active areas only moves the CF peaks closer to the solar surface. However, the 17 GHz τ results (orange curves) in the umbral region showed a huge change in the TR structure that cannot be attributed to free-free opacity and will be discussed in detail in the next **Section 4.2**. The chromospheric free-free contribution is still present at 17 GHz, but its CF peak is only 5% of the TR peak (see the small orange peak close to 800 km).

4.2 Gyroresonance Contribution

Several studies (e.g., Shibasaki et al., 1994; White and Kundu, 1997; Kundu et al., 2001; Vourlidas et al., 2006) have established that the gyroresonance radio emission is produced by opacity in harmonics 2, 3 and 4 of the electron cyclotron frequency, necessarily at TR or coronal heights in order to produce the brightness temperatures in excess of 10^5 K observed at 17 GHz. Moreover, Vourlidas et al. (2006) suggested that ARs with high polarization ($\geq 30\%$) at 17 GHz have gyroresonance cores, and that $|\vec{B}| = 2200$ G is the minimum intensity to generate such a core. AR 12470 presented a component with high polarization degree (up to 94%) and $|\vec{B}| \sim 2500$ G that is likely to be due to a gyroresonance source.

To investigate the gyroresonance contribution, κ_g was calculated for harmonics $s \leq 5$, allowing for an uncertainty of 10% in the $|\vec{B}|$ values. That is, the 3rd harmonic was calculated where the magnetic field model showed intensities of $|\vec{B}| \approx 2000 \pm 200$ G, the 4th harmonic was calculated where $|\vec{B}| \approx 1500 \pm 150$ G, and the 5th harmonic where $|\vec{B}| \approx 1200 \pm 120$ G. Due to the heliographic position of AR 12740 (17.40°N, 17.68°E), it is estimated that $|\vec{B}|$ is 7.5% greater than the observed B_z .

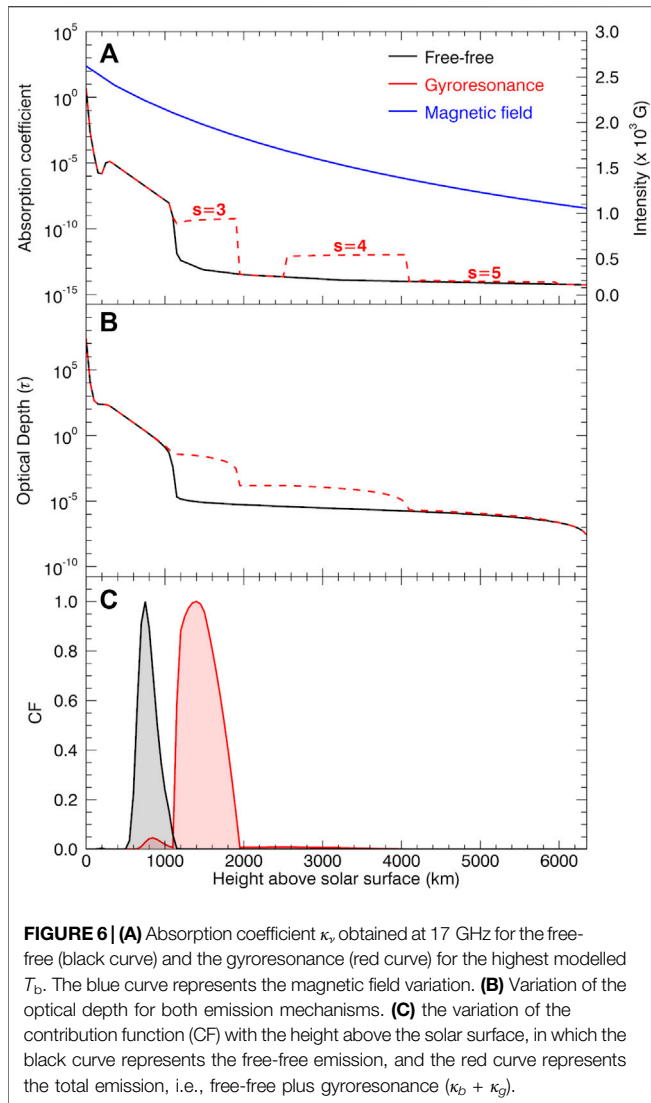
Figure 6A shows the variation in the absorption coefficient κ , with height along the line-of-sight to the location of maximum brightness temperature in AR 12470. The blue curve represents the magnetic field variation with height. The continuous black curve shows the absorption coefficient for bremsstrahlung (κ_b),

and the dashed curve, in red, represents the contribution of gyroresonance ($\kappa_v = \kappa_b + \kappa_g$) and each of its respective harmonics (s). The 3rd harmonic occurs between 1,150 and 1,900 km in altitude, while the 4th harmonic occurs between 2,550 and 4,050 km. As for the 5th harmonic, it occurs between 4,250 and 5,950 km.

Figure 6B shows the τ variation with the height, where the 3rd and 4th harmonics effectively contribute to τ . The 3rd harmonic provides an optical depth of $\tau \sim 10^{-1}$ (**Figure 6B** red curve) that is three orders of magnitude greater than the free-free optical depth (**Figure 6B** black curve). The contribution from the 4th harmonic is an order of magnitude larger than the free-free τ . These results are in agreement with the studies of Shibasaki et al. (1994), who found that the 3rd harmonic contribution is approximately three orders of magnitude greater than the 4th harmonic. Despite being optically thin, the gyroresonance contribution of $\tau \sim 10^{-1}$ is able to increase the 17 GHz T_b from 10×10^3 K to almost 70×10^3 K thanks to the high temperature in the gyroresonance layers. To illustrate the contribution of each mechanism at 17 GHz, **Figure 6C** shows the free-free CF in black and the total CF in red (free-free plus gyroresonance). While the free-free CF shows a single peak at around 800 km (black curve), when the gyroresonance is included an intense peak appears at TR/coronal heights (red curve) that is ~ 20 times greater than the free-free contribution.

4.3 Comparison of the Synthetic and Observed Radio Images

The GA model images were generated with $2''$ spatial resolution, which is much finer than the resolution of the radio observations. To compare the simulations with the observations, the model results were convolved with a 2D Gaussian beam that matches the resolution of the ALMA single-dish observations, i.e., $25''$ and $58''$



at 230 and 100 GHz, respectively. In **Figure 7** the 2D structure of AR 12470 observed with ALMA at 230 and 100 GHz (left panels) is compared with the model results (right panels). The upper row shows the 100 GHz comparison, while the lower row shows the 230 GHz comparison.

Due to better spatial resolution, the 230 GHz map shows more detail than that observed at 100 GHz, in both observation and model. The bright features observed at both frequencies are in good agreement with the simulations. Moreover, due to the small size of the sunspot umbra (25'' diameter at its widest), the dark umbral structure is readily seen at 230 GHz (see the center of panels **Figures 7C,D**), but completely masked in the 100 GHz simulations due to the convolution with the bright structures around it (see **Figures 7A,B**).

Even though dark when compared with the surrounding areas, the umbral T_b is only smaller than the $T_{b,QS}$ in the 230 GHz observation, and in the model result without the beam convolution, as shown in **Table 3**. When convolved to the observational resolution of 25'', the modelled umbral T_b at

230 GHz is at the same level as $T_{b,QS}$. Furthermore, as shown in **Table 3**, the other AR areas (penumbra and plages) are brighter than the quiet Sun and showed a greater T_b variation than the umbra. All the simulated areas are consistent with the observations to within the uncertainties.

The resulting low contrast of the dark umbra with respect to the quiet Sun in the model is due to the low resolution of the ALMA single-dish observations. Since the umbral size is almost equal to the ALMA 230 GHz beam, the umbral T_b is smoothed with the bright surrounding areas. At the much better resolution of the ALMA interferometric array, the AR 12470 umbra presented brightness temperature as low as $\sim 0.90 \times T_{qS}$ (see Shimojo et al., 2017). Additionally, the 100 GHz ALMA interferometric observations obtained on 16 December 2015 showed a mysterious bright structure inside the umbra (Iwai et al., 2017; Brajša et al., 2021) that may still be present on December 17, increasing the umbral T_b and consequently the modeled value.

Figure 8 compares the observation obtained at 17 GHz by NoRH (8a) with the model results. Due to the high T_b in the polarized region ($\sim 7.0 \times T_{qS}$), to visualize the other regions the image display range was saturated at $3.0 \times T_{qS}$, allowing us to see bright free-free structures at positions consistent with those in the ALMA maps. Away from the polarized region, the maximum T_b was close to $2.8 \times T_{qS}$, and the average value was $1.58 \pm 0.32 \times T_{qS}$ (see **Table 4**).

At 17 GHz the non-polarized regions appear in the model at positions matching the observed ones. However, the modeled atmospheric profiles that achieved good agreement with the T_b observations at 230 and 100 GHz were not able to reach the high T_b values observed at 17 GHz. While these regions showed observational values as high as $2.8 \times T_{qS}$, the model was only able to reach a maximum T_b of $1.2 \times T_{qS}$ (**Figure 8B**). Moreover, since each modeled pixel used the same form of atmospheric profile to model the 3 frequencies (230, 100, and 17 GHz), we might expect the model to show good agreement with the bright and dark regions. The free-free regions bright at 17 GHz in the model (**Figure 8B**) have good spatial agreement with those ones modeled at 230 and 100 GHz (**Figures 7B,D**).

If only free-free emission is considered, at 17 GHz the umbra appears darker in the model than the surrounding area, with a brightness temperature of $1.06 \pm 0.02 \times T_{qS}$ at 10'' resolution. When gyroresonance is included, the modeled T_b increased to values above $10 \times T_{qS}$. As summarized in **Table 4**, when gyroresonance is taken into account the T_b values obtained for the highly polarized region are in agreement with those observed. Nevertheless, as can be observed in **Figure 3**, the shape of the modelled polarized region is smaller and rounder, while the observed source appears elliptical.

5 CONCLUDING REMARKS

In this work, we present a data-constrained model of the solar atmosphere, in which we used the brightness temperatures of AR NOAA 12470 observed at three radio frequencies: 17 GHz

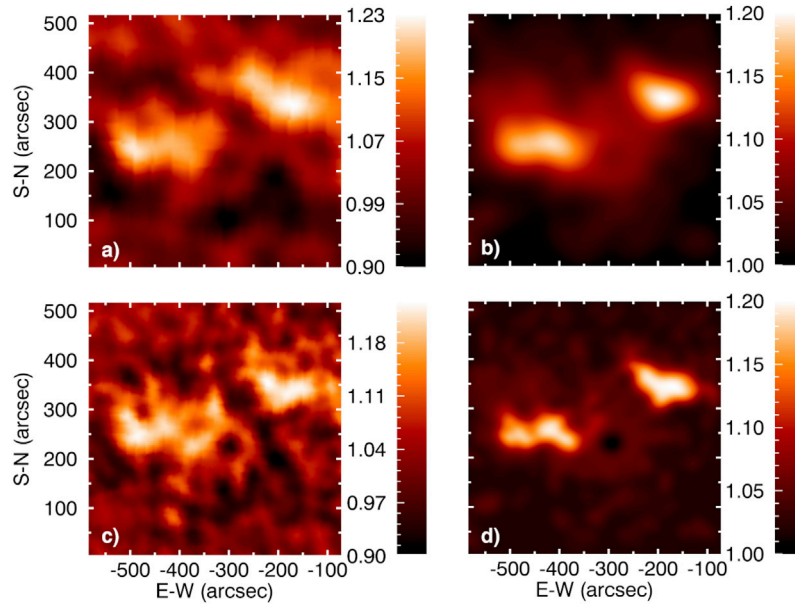


FIGURE 7 | Comparison between the observations and the model results at ALMA wavelengths. The upper panels show the 100 GHz comparison between the **(A)** ALMA observation and the **(B)** model results convolved with a gaussian beam of $58''$ resolution. The lower panels show **(C)** the ALMA observation at 230 GHz and **(D)** the model results convolved with a $25''$ gaussian beam. As in **Table 3**, the color bar scale is in multiples of the value of $T_{b,GS}$ appropriate for each frequency.

TABLE 3 | Comparison of the ALMA observations at 230 and 100 GHz and modeled averaged brightness temperatures of the distinct AR areas as compared with the quiet Sun temperature ($T_{b,GS}$).

AR region	Averaged brightness temperature ($\times T_{GS}$)					
	230 GHz			100 GHz		
	Obs	Model		Obs	Model	
	$2''$	$25''$		$2''$	$58''$	
Umbral	0.99 ± 0.04	0.98 ± 0.01	1.00 ± 0.01	1.03 ± 0.01	1.02 ± 0.01	1.06 ± 0.01
Penumbra	1.05 ± 0.05	1.04 ± 0.01	1.02 ± 0.02	1.05 ± 0.02	1.07 ± 0.01	1.07 ± 0.02
Plages	1.07 ± 0.07	1.08 ± 0.05	1.04 ± 0.04	1.06 ± 0.04	1.10 ± 0.04	1.06 ± 0.03

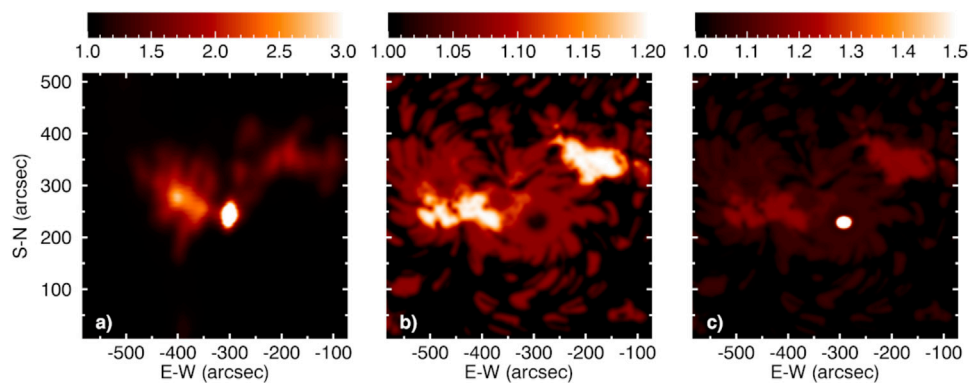


FIGURE 8 | **(A)** NoRH observation of AR 12470 at 17 GHz, with the displayed intensities saturating at $3 \times T_{GS}$ K (i.e., well below the peak T_b of the highly polarized source). **(B)** The GA model image at 17 GHz with $10''$ resolution based only on the free-free opacity, and **(C)** the GA model result when both free-free and gyroresonance are included. As in **Table 4**, the color bar scale is in multiples of $T_{b,GS}$ at 17 GHz (10,000 K).

TABLE 4 | Comparison of the 17 GHz observation and modeled averaged brightness temperatures of the polarized and non-polarized regions.

Bright region	Averaged brightness temperature at 17 GHz ($\times T_{qS}$)				
	Obs	κ_b		$\kappa_b + \kappa_g$	
		Model	2"	10"	Model
Polarized	3.69 ± 1.35	1.06 ± 0.03	1.06 ± 0.02	9.41 ± 3.51	4.08 ± 1.19
Non-polarized	1.58 ± 0.32	1.04 ± 0.06	1.04 ± 0.06	1.04 ± 0.06	1.04 ± 0.05

from NoRH, and 100 and 230 GHz from ALMA single-dish data. Under the assumption that the radio emission originates from the combination of thermal free-free and gyroresonance processes, our model allows for calculating radio brightness temperature maps that can be compared with the observations. The magnetic field at distinct atmospheric heights was determined by a force-free field extrapolation using HMI/SDO photospheric magnetograms. In order to determine the best plasma temperature and density height profiles necessary to match the observations, the Pikaia genetic algorithm (Charbonneau, 1995) is used to modify the standard quiet Sun atmospheric model characterized by 5 free parameters: the chromospheric gradients of temperature and electron density, the coronal temperature and density, and the TR height. The SSC (Selhorst et al., 2005b) was used as the basic quiet Sun model, however, other models could be chosen as the basic model. The GA modified the SSC model to fit three distinct classes of active region features, defined by their magnetic field intensities: umbrae, penumbrae, and plages.

As seen in **Figure 7** and **Table 3**, at the ALMA wavelengths the model was in general agreement with the observations. The umbral region looks dark at 230 GHz and the brighter regions match the positions seen in the observations at both frequencies (230 and 100 GHz). However, due to the small size of the umbra (diameter $\leq 25''$), it is not apparent in the 100 GHz data or model. Moreover, as shown by the ALMA interferometric observations at 230 GHz (Shimojo et al., 2017), the umbral region is darker ($\sim 0.90 \times T_{qS}$) than the single dish maps show ($0.99 \pm 0.04 \times T_{qS}$), implying that the umbra will be darker at 100 and 17 GHz. Nevertheless, there are no observational data to confirm that. While at 17 GHz the umbral free-free emission is masked by the bright source due to gyroresonance opacity, at 100 GHz, the interferometric image showed the presence of a bright structure inside the umbral region (Iwai et al., 2017), that may be produced higher in the atmosphere than the region where the umbral emission is formed.

Since the umbra is the region with the greatest magnetic field intensity ($|\vec{B}|$), it is also the location where the 17 GHz gyroresonance emission arises. As reported in previous works (Shibasaki et al., 1994; Vourlidis et al., 2006; Selhorst et al., 2008), gyroresonance emission at 17 GHz is typically formed at the 3rd harmonic ($|\vec{B}| = 2000$ G), and needs to be well above the TR where the free-free emission is optically thin. However, the free-free contribution function is much smaller than that of

the gyroresonance (**Figure 6C**). Moreover, if only thermal free-free emission was contributing opacity at 17 GHz, the AR umbra should look darker than the surrounding region (see **Figure 8B**) and probably darker than the quiet Sun as the high resolution ALMA interferometric data suggest.

DATA AVAILABILITY STATEMENT

The original contributions presented in the study are included in the article/supplementary material, further inquiries can be directed to the corresponding author.

AUTHOR CONTRIBUTIONS

AJOS, CLS, and JERC contributed to conception and design of the study. CLS and PJAS wrote the first draft of the manuscript. All authors contributed to manuscript revision, read, and approved the submitted version.

FUNDING

This research was partially supported from the São Paulo Research Foundation (FAPESP) grant Nos. 2013/10559-5, 2013/24155-3 and 2019/03301-8. PJAS acknowledges support from CNPq (contract 307612/2019-8). SW was supported by the SolarALMA project, which has received funding from the European Research Council (ERC) under the European Union's Horizon 2020 research and innovation programme (grant agreement No. 682462), and by the Research Council of Norway through its Centres of Excellence scheme, project number 262622.

ACKNOWLEDGMENTS

This paper makes use of the following ALMA data: ADS/JAO.ALMA#2011.0.00020.SV. ALMA is a partnership of ESO (representing its member states), NSF (United States) and NINS (Japan), together with NRC (Canada) and NSC and ASIAA (Taiwan), and KASI (Republic of Korea), in co-operation with the Republic of Chile. The Joint ALMA Observatory is operated by ESO, AUI/NRAO, and NAOJ. The

National Radio Astronomy Observatory is a facility of the National Science Foundation operated under cooperative agreement by Associated Universities, Inc. AV acknowledges financial support from the FAPESP, grant No. 2013/10559-5 CGGC is grateful with FAPESP (2013/

24155-3), CAPES (88887.310385/2018-00) and CNPq (307722/2019-8). RB acknowledges the support by the Croatian Science Foundation under the project 7549 “Millimeter and sub-millimeter observations of the solar chromosphere with ALMA.”

REFERENCES

- Brajsa, R., Romštajn, I., Wöhl, H., Benz, A. O., Temmer, M., and Roša, D. (2009). Heights of Solar Tracers Observed at 8 Mm and an Interpretation of Their Radiation. *Astronomy Astrophysics* 493, 613–621. doi:10.1051/0004-6361/200810299
- Brajsa, R., Skokic, I., Sudar, D., Benz, A. O., Krucker, S., Ludwig, H.-G., et al. (2021). ALMA Small-Scale Features in the Quiet Sun and Active Regions. *Astronomy Astrophysics* 651, A6. doi:10.1051/0004-6361/201936231
- Brajsa, R., Skokic, I., and Sudar, D. (2020). Magnetic Structure above Solar Active Regions. *Cent. Eur. Astrophys. Bull.* 44, 1.
- Brajsa, R., Sudar, D., Benz, A. O., Skokic, I., Bárta, M., De Pontieu, B., et al. (2018). First Analysis of Solar Structures in 1.21 Mm Full-Disc ALMA Image of the Sun. *Astronomy Astrophysics* 613, A17. doi:10.1051/0004-6361/201730656
- Charbonneau, P. (1995). Genetic Algorithms in Astronomy and Astrophysics. *ApJS* 101, 309. doi:10.1086/192242
- Dulk, G. A. (1985). Radio Emission from the Sun and Stars. *Annu. Rev. Astron. Astrophys.* 23, 169–224. doi:10.1146/annurev.aa.23.090185.001125
- Fontenla, J. M., Avrett, E. H., and Loeser, R. (1993). Energy Balance in the Solar Transition Region. III - Helium Emission in Hydrostatic, Constant-Abundance Models with Diffusion. *ApJ* 406, 319–345. doi:10.1086/172443
- Fontenla, J. M., Curdt, W., Haberleiter, M., Harder, J., and Tian, H. (2009). Semiempirical Models of the Solar Atmosphere. III. Set of Non-LTE Models for Far-Ultraviolet/Extreme-Ultraviolet Irradiance Computation. *ApJ* 707, 482–502. doi:10.1088/0004-637X/707/1/482
- Fontenla, J., White, O. R., Fox, P. A., Avrett, E. H., and Kurucz, R. L. (1999). Calculation of Solar Irradiances. I. Synthesis of the Solar Spectrum. *ApJ* 518, 480–499. doi:10.1086/307258
- Iwai, K., Koshiishi, H., Shibasaki, K., Nozawa, S., Miyawaki, S., and Yoneya, T. (2016). Chromospheric Sunspots in the Millimeter Range as Observed by the Nobeyama Radioheliograph. *ApJ* 816, 91. doi:10.3847/0004-637X/816/2/91
- Iwai, K., Shimojo, M., Asayama, S., Minamidani, T., White, S., Bastian, T., et al. (2017). The Brightness Temperature of the Quiet Solar Chromosphere at 2.6 Mm. *Sol. Phys.* 292, 22. doi:10.1007/s11207-016-1044-5
- Iwai, K., and Shimojo, M. (2015). Observation of the Chromospheric Sunspot at Millimeter Range with the Nobeyama 45 M Telescope. *ApJ* 804, 48. doi:10.1088/0004-637X/804/1/48
- Kaufmann, P., Levato, H., Cassiano, M. M., Correia, E., Costa, J. E. R., Giménez de Castro, C. G., et al. (2008). “New Telescopes for Ground-Based Solar Observations at Submillimeter and Mid-infrared,” in *Ground-based and Airborne Telescopes II. Vol. 7012 of Society of Photo-Optical Instrumentation Engineers (SPIE) Conference Series*. Editors L. M. Stepp and R. Gilmozzi, 70120L. doi:10.1117/12.788889
- Kundu, M. R., White, S. M., Shibasaki, K., and Raulin, J. P. (2001). A Radio Study of the Evolution of Spatial Structure of an Active Region and Flare Productivity. *Astrophys. J. Suppl. S* 133, 467–482. doi:10.1086/320351
- Livingston, W., Penn, M. J., and Svalgaard, L. (2012). Decreasing Sunspot Magnetic Fields Explain Unique 10.7 Cm Radio Flux. *ApJ* 757, L8. doi:10.1088/2041-8205/757/1/L8
- Loukitcheva, M., Solanki, S. K., and White, S. M. (2014). The Chromosphere above Sunspots at Millimeter Wavelengths. *Astronomy Astrophysics* 561, A133. doi:10.1051/0004-6361/201321321
- Nakagawa, Y., and Raadu, M. A. (1972). On Practical Representation of Magnetic Field. *Sol. Phys.* 25, 127–135. doi:10.1007/BF00155751
- Nakajima, H., Nishio, M., Enome, S., Shibasaki, K., Takano, T., Hanaoka, Y., et al. (1994). The Nobeyama Radioheliograph. *Proc. IEEE* 82, 705–713. doi:10.1109/5.284737
- Nita, G. M., Fleishman, G. D., Kuznetsov, A. A., Kontar, E. P., and Gary, D. E. (2015). Three-dimensional Radio and X-Ray Modeling and Data Analysis Software: Revealing Flare Complexity. *ApJ* 799, 236. doi:10.1088/0004-637X/799/2/236
- Nita, G. M., Viall, N. M., Klimchuk, J. A., Loukitcheva, M. A., Gary, D. E., Kuznetsov, A. A., et al. (2018). Dressing the Coronal Magnetic Extrapolations of Active Regions with a Parameterized Thermal Structure. *ApJ* 853, 66. doi:10.3847/1538-4357/aaa4bf
- Pesnell, W. D., Thompson, B. J., and Chamberlin, P. C. (2012). The Solar Dynamics Observatory (SDO). *Sol. Phys.* 275, 3–15. doi:10.1007/s11207-011-9841-3
- Schou, J., Borrero, J. M., Norton, A. A., Tomczyk, S., Elmore, D., and Card, G. L. (2012). Polarization Calibration of the Helioseismic and Magnetic Imager (HMI) Onboard the Solar Dynamics Observatory (SDO). *Sol. Phys.* 275, 327–355. doi:10.1007/s11207-010-9639-8
- Seehafer, N. (1978). Determination of Constant ? Force-free Solar Magnetic Fields from Magnetograph Data. *Sol. Phys.* 58, 215–223. doi:10.1007/bf00157267
- Selhorst, C. L., Costa, J. E. R., and Silva, A. V. R. (2005a). “3-D Solar Atmospheric Model over Active Regions,” in *ESA SP-600: The Dynamic Sun: Challenges for Theory and Observations*.
- Selhorst, C. L., Silva, A. V. R., and Costa, J. E. R. (2005b). What Determines the Radio Polar Brightening? *Astronomy Astrophysics* 440, 367–371. doi:10.1051/0004-6361:20053083
- Selhorst, C. L., Silva-Válio, A., and Costa, J. E. R. (2009). “17 GHz Active Region Model Using Magnetogram Extrapolation,” in *The Second Hinode Science Meeting: Beyond Discovery-Toward Understanding. Vol. 415 of Astronomical Society of the Pacific Conference Series*. Editors B. Lites, M. Cheung, T. Magara, J. Mariska, and K. Reeves, 207.
- Selhorst, C. L., Silva-Válio, A., and Costa, J. E. R. (2008). Solar Atmospheric Model over a Highly Polarized 17 GHz Active Region. *Astronomy Astrophysics* 488, 1079–1084. doi:10.1051/0004-6361:20079217
- Selhorst, C. L., Simões, P. J. A., Brajsa, R., Valio, A., de Castro, C. G. G., Costa, J. E. R., et al. (2019). Solar Polar Brightening and Radius at 100 and 230 GHz Observed by ALMA. *ApJ* 871, 45. doi:10.3847/1538-4357/aaf4f2
- Shibasaki, K., Enome, S., Nakajima, H., Nishio, M., Takano, T., Hanaoka, Y., et al. (1994). A Purely Polarized S-Component at 17 GHz. *PASJ* 46, L17–L20.
- Shimojo, M., Bastian, T. S., Hales, A. S., White, S. M., Iwai, K., Hills, R. E., et al. (2017). Observing the Sun with the Atacama Large Millimeter/submillimeter Array (ALMA): High-Resolution Interferometric Imaging. *Sol. Phys.* 292, 87. doi:10.1007/s11207-017-1095-2
- Silva, A. V. R., Laganá, T. F., De Castro, C. G. G., Kaufmann, P., Costa, J. E. R., Levato, H., et al. (2005). Diffuse Component Spectra of Solar Active Regions at Submillimeter Wavelengths. *Sol. Phys.* 227, 265–281. doi:10.1007/s11207-005-2787-6
- Takano, T., Nakajima, H., Enome, S., Shibasaki, K., Nishio, M., Hanaoka, Y., et al. (1997). “An Upgrade of Nobeyama Radioheliograph to a Dual-Frequency (17 and 34 GHz) System,” in *Coronal Physics from Radio and Space Observations. Vol. 483 of Lecture Notes in Physics*. Editor G. Trotter (Berlin: Springer-Verlag), 183–191. doi:10.1007/BFb0106457
- Tapia-Vázquez, F., and De la Luz, V. (2020). Nonlinear Convergence of Solar-like Stars Chromospheres Using Millimeter, Submillimeter, and Infrared Observations. *ApJS* 246, 5. doi:10.3847/1538-4365/ab5f0a
- Valle Silva, J. F., Giménez de Castro, C. G., Selhorst, C. L., Raulin, J.-P., and Valio, A. (2020). Spectral Signature of Solar Active Region in Millimetre and Submillimetre Wavelengths. *MNRAS* 500, 1964–1969. doi:10.1093/mnras/staa3354
- Vernazza, J. E., Avrett, E. H., and Loeser, R. (1981). Structure of the Solar Chromosphere. III - Models of the EUV Brightness Components of the Quiet-Sun. *ApJS* 45, 635–725. doi:10.1086/190731

- Vourlidis, A., Gary, D. E., and Shibasaki, K. (2006). Sunspot Gyroresonance Emission at 17 GHz: A Statistical Study. *Publ. Astron. Soc. Jpn.* 58, 11–20. doi:10.1093/pasj/58.1.11
- Wedemeyer, S., Bastian, T., Brajša, R., Hudson, H., Fleishman, G., Loukitcheva, M., et al. (2016). Solar Science with the Atacama Large Millimeter/Submillimeter Array-A New View of Our Sun. *Space Sci. Rev.* 200, 1–73. doi:10.1007/s11214-015-0229-9
- White, S. M., Iwai, K., Phillips, N. M., Hills, R. E., Hirota, A., Yagoubov, P., et al. (2017). Observing the Sun with the Atacama Large Millimeter/submillimeter Array (ALMA): Fast-Scan Single-Dish Mapping. *Sol. Phys.* 292, 88. doi:10.1007/s11207-017-1123-2
- White, S. M., and Kundu, M. R. (1997). Radio Observations of Gyroresonance Emission from Coronal Magnetic Fields. *Sol. Phys.* 174, 31–52. doi:10.1023/a:1004975528106
- Zirin, H. (1988). in *Astrophysics of the Sun* (New York, EUA: Cambridge University Press).
- Zlotnik, E. Y., Kundu, M. R., and White, S. M. (1996). A Model of the Atmosphere above a Sunspot from Radio Observations. *Radiophys. Quantum Electron* 39, 255–267. doi:10.1007/BF02144449

Conflict of Interest: The authors declare that the research was conducted in the absence of any commercial or financial relationships that could be construed as a potential conflict of interest.

Publisher's Note: All claims expressed in this article are solely those of the authors and do not necessarily represent those of their affiliated organizations, or those of the publisher, the editors and the reviewers. Any product that may be evaluated in this article, or claim that may be made by its manufacturer, is not guaranteed or endorsed by the publisher.

Copyright © 2022 de Oliveira e Silva, Selhorst, Costa, Simões, Giménez de Castro, Wedemeyer, White, Brajša and Valio. This is an open-access article distributed under the terms of the Creative Commons Attribution License (CC BY). The use, distribution or reproduction in other forums is permitted, provided the original author(s) and the copyright owner(s) are credited and that the original publication in this journal is cited, in accordance with accepted academic practice. No use, distribution or reproduction is permitted which does not comply with these terms.